Chapter 5

Electronic, Transport and Magnetic Properties of Cr-based Chalcogenide Spinels

Chuan-Chuan Gu, Xu-Liang Chen and
Zhao-Rong Yang

Additional information is available at the end of the chapter

http://dx.doi.org/10.5772/110953

Abstract

The Cr-based chalcogenide spinels with general formula ACr_2X_4 (A = Cd, Zn, Hg, Fe; X = S, Se) host rich physical properties due to coexistence of frustration as well as strong coupling among spin, charge, orbital and lattice degrees of freedom. In this chapter, recent advances on the study of electronic transport and magnetic properties of ACr_2X_4 are reviewed. After a short introduction of the crystal structure and magnetic interactions, we focus on the colossal magnetoresistance (CMR) in $FeCr_2S_4$, colossal magnetocapacitance (CMC) in $CdCr_2S_4$, negative thermal expansion (NTE) in $ZnCr_2Se_4$ and complex orbital states in $FeCr_2S_4$. It is hoped that this chapter will be beneficial for the readers to explore the interplay among different degrees of freedom in the frustrated system.

Keywords: Cr-based spinel, colossal magnetoresistance, colossal magnetocapacitance, negative thermal expansion, frustrated magnet, complex orbital states

1. Introduction

Chromium-based chalcogenide spinels with general formula ACr_2X_4 (A = Cd, Zn, Hg, Fe; X = S, Se) have attracted special attention not only for pure academic interest, but also for potential applications [1–4]. On the one hand, the chromium-based chalcogenide spinels are typical strongly correlated electron materials. Due to strong coupling among spin, charge, orbital and lattice degrees of freedom, this system displays rich physical properties such as colossal magnetoresistance (CMR), colossal magnetocapacitance (CMC), gigantic Kerr rotation, and magnetoelectric effect [5–8]. On the other hand, the existence of frustration

(magnetic or orbital frustration) increases complexity of the system, yielding complex behaviors such as spin glass, orbital glasses, and spin nematic [9–11]. Depending on external perturbation from magnetic field, electric field, chemical substitution, or disorder, different quantum states are subtle balanced, increasing difficulty for understanding the intrinsic physics of this system. For example, the polycrystalline (PC) sample of $FeCr_2S_4$ displays orbital ordering around 9K, while single crystal (SC) sample shows orbital glass [12, 13]. $CdCr_2S_4$ single crystal exhibits multiferroic behavior with the evidence of relaxor ferroelectricity and CMC [6]. However, the emergence of ferroelectricity and CMC effect in these thio-spinels was found to be highly sensitive to the detail of sample preparation and chemical doping. Both multiferroicity and CMC effect are absent in PC samples [14].

In this chapter, recent progresses in the studies of Cr-based chalcogenide spinels are described. We will focus on the origin of several physical effects including CMR, CMC and NTE. The origin of complex spin and orbital states will also be covered.

2. Crystal structure and magnetic interactions in ACr_2X_4 (A= Cd, Zn, Hg, Fe; X = S, Se)

The chromium-based spinels ACr_2X_4 (A = Cd, Zn, Hg, Fe; X = S, Se) have the cubic symmetry with space group $Fd3'm$ (O_h^7), as is shown in **Figure 1**. Each cubic cell has 8 molecular formulae, which possess 56 ions, including 8 A^{2+} ions, 16 Cr^{3+} ions and 32 X^{2-} ions. The X^{2-} anions form a close-packed face-centered cubic lattice with two-type coordinated interstice: tetrahedral and octahedral ones. In the normal type spinel, the A^{2+} ions occupy 1/8 of the tetrahedrally coordinated interstices and the B^{3+}ions occupy 1/2 of the octahedrally coordinated interstices. Otherwise, it is defined as an inverse spinel type, in which the A^{2+} and B^{3+} cations exchange the sites. In some situations, the compound with the same chemical elements could be formed by normal and inverse type spinel simultaneously [15, 16].

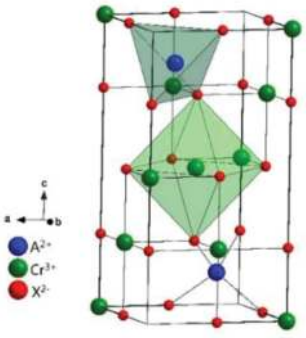

Figure 1. Schematic structure of spinel ACr_2X_4. A^{2+} ions are in tetrahedral and Cr^{3+} ions in octahedral site.

http://dx.doi.org/10.5772/110953

In ACr_2X_4, if magnetic cations (such as Mn^{2+}, Co^{2+}, Fe^{2+}) occupy the A site, the system usually displays a ferrimagnetic order with a net magnetization, due to the opposite spin direction of A and B sites. On the other hand, if A site is occupied by nonmagnetic ions (e.g., Zn^{2+}, Cd^{2+}, Hg^{2+}), the Cr^{3+} ions form a network of corner-sharing tetrahedral known as the pyrochlore lattice [17]. The dominant frustration in this network that hinders a simple antiparallel spin pattern is tightly associated with the way the Cr-Cr atoms are separated. The different ground states as a function of lattice constants are driven by the dominating exchange interactions: at small Cr-Cr separation, strong direct antiferromagnetic (AFM) exchange dominates, indicative of strong geometrical frustration [18]; at larger Cr-Cr separations, 90° Cr^{3+}-X^{2-}-Cr^{3+} ferromagnetic and Cr^{3+}-X^{2-}-A^{2+}-X^{2-}-Cr^{3+} or AFM Cr^{3+}-X^{2-}-X^{2-}-Cr^{3+} superexchange interactions come into play [1], with additional bond frustration dominanting in the sulfides and selenides.

3. Colossal magnetoresistance in $FeCr_2S_4$

The presence of the CMR effect in mixed valence manganese oxides $R^{3+}_{1-x}A^{2+}_{x}MnO_3$ (R is a rare earth and A is a divalent alkaline earth) in the vicinity of a paramagnetic (PM) to ferromagnetic (FM) transition has been the subject of much recent interest [19, 20]. This conductive behavior is described by the double-exchange (DE) model [21], which suggests that the conductivity is decided by the hopping of the electrons between hetrovalent Mn^{3+}/Mn^{4+} pairs [22]. Later, another CMR material—$FeCr_2S_4$ has been reported by Ramirez et al. [5]. Since the magneto-transport behaviors of $FeCr_2S_4$ are quite similar to manganite perovskites, one might expect to apply the DE theory and Jahn-Teller (JT) polaron mechanism to explain the CMR effects in $FeCr_2S_4$. However, the X-ray diffraction (XRD) pattern and Mössbauer spectrum give direct evidences that there is no DE mechanism in $FeCr_2S_4$ [23].

The magnetization (M) in the temperature range from 4.2 to 400 K at the field H = 0.01 T is shown in **Figure 2(a)**. With decreasing temperature, M first increases slowly, and then increases abruptly near T_C^{onset} (173 K) due to the PM-FM transition. The Curie temperature T_C is 168 K,

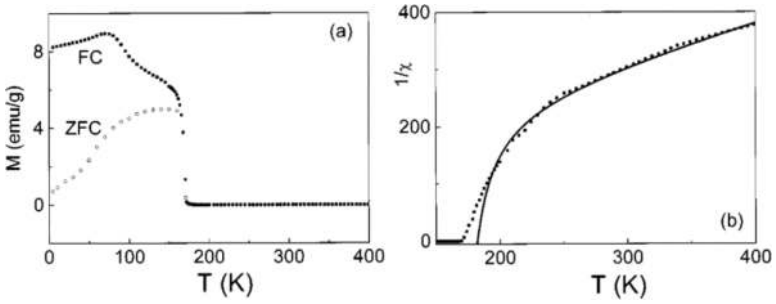

Figure 2. (a) Temperature dependence of the magnetization in field-cooled (FC) and zero-field-cooled (ZFC) sequences, respectively and (b) temperature dependence of the paramagnetic susceptibility χ as a plot of $1/\chi$ versus temperature [24].

which is defined as the temperature corresponding to maximum of $|dM/dT|$. To clarify the magnetism in $FeCr_2S_4$, the temperature dependence of the PM susceptibility χ is shown in **Figure 2(b)** as a plot of $1/\chi$ versus temperature. According to the physics of ferrimagnetism, the temperature dependence of the PM susceptibility χ can be described by Eq. (1) [25, 26]:

$$1/\chi = T/C + 1/\chi_0 - \sigma/(T-\theta). \tag{1}$$

Here χ_0, C, σ and θ are fitting parameters. The fit results of χ are shown as the solid line in **Figure 2(b)**, with $1/\chi_0 = 130(\pm 2)$, $C = 1.50(\pm 0.02)$, $\sigma = 3818(\pm 50)$ and $\theta = 167(\pm 3)$. Clearly, Eq. (1) fits the experimental result well except near T_C, indicating a ferrimagnet state. At temperatures near and above T_C, the system has strong short-range magnetic correlation, thus not in an ideal PM state.

The temperature-dependent resistivity ρ and magnetoresistance $MR_H = [\rho(0) - \rho(H)]/\rho(0)$ from 4.2 K to 300 K under three different applied fields (0, 3 and 5 T) are shown in **Figure 3**. Both ρ and MR_H display a peak near T_C^{onset}. The maximum of MR_5 is 16%. The temperature corre-

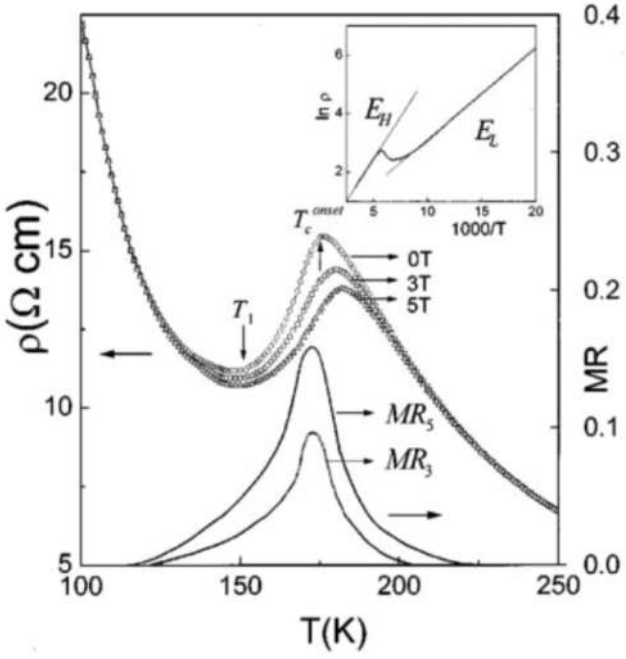

Figure 3. Resistivity ρ and magnetoresistance $MR_H = [\rho(0) - \rho(H)]/\rho(0)$, versus temperature for $FeCr_2S_4$. The inset shows the curve of ln ρ versus $1000/T$ [24].

sponding to the minimum resistivity in the ρ-T curve below T_C is defined as T_1 = 153 K. As seen from the inset of **Figure 3**, the curve of ln ρ versus 1000/T is linear at both $T > T_C^{onset}$ and $T < T_1$, indicating a semiconductor like behavior in two regions. The fits by $\rho = \rho_0 \exp(E/k_BT)$ give the activation energies E_L = 26 meV for $T < T_1$, and E_H = 47 meV for $T > T_C^{onset}$, respectively. This implies that the conduction mechanisms are different for the two temperature regions. $E_H > E_L$ indicates clearly that E_H, the activated energy at temperatures above T_C^{onset}, does not arise from a simple thermally activated effect. In order to understand the discrepancy between E_L and E_H, the thermoelectric power (S) is fitted by the experimental data through $S = (k_B/e)(a + E_S/k_BT)$ [24, 27]. E_S is obtained as 23 meV, which is approximately equal to 26 meV for E_L, and much lower than 47 meV for E_H. The discrepancy between E_S and E_H in manganite perovskites can be attributed to the presence of lattice or magnetic polarons. Since there is neither a structure transition nor a JT effect around T_C in $FeCr_2S_4$, the polarons mainly exist in the form of magnetic polarons [28].

The sample at temperatures above T_C^{onset} is in a typical PM state, in favor of the existence of magnetic polarons [24]. As is known, a magnetic polaron is a carrier coupled by short-range magnetic correlation within a magnetic cluster at temperatures above T_C^{onset}. Thus, the effective mass of a magnetic polaron increases greatly with respect to that of a naked carrier, which means it has a lower mobility and a higher activated energy [29, 30]. In an ideal FM order, magnetic polarons will be delocalized from the self-trapped state and turn into naked carriers completely [29]. In consequence, ρ decreases drastically at this point, accompanied with the system changing completely to one of thermal-activated transport of naked carriers. However, ρ decreases gradually from T_C^{onset} to T_1, and MR also expands to a broader temperature range below T_C^{onset}, indicative of the existence of magnetic polarons in this temperature range. Magnetic polarons will be delocalized gradually as the PM phase weakens. They then vanish completely at T_1, denoting that magnetic order destroys the environment for magnetic polarons. Hence, ρ in the temperature range from T_C^{onset} to T_1 can be described by a two-fluid model involving the coexistence of magnetic polarons and naked carriers. It could also explain that MR expands to a broader temperature range below T_C^{onset}, since the formation of magnetic polarons is inhibited by the enhancement of FM order at an external magnetic field.

To further investigate the evolution of magnetic polarons in $FeCr_2S_4$, nonmagnetic Cd is substituted for Fe. The XRD measurement for $Fe_{1-x}Cd_xCr_2S_4$ reveals that the substitution of Fe by Cd produces no structural change [31]. The resistivity ρ and magnetoresistance $MR_H = [\rho(0) - \rho(H)]/\rho(0)$, as a function of temperature are shown in **Figure 4**. Comparing with $FeCr_2S_4$, the Cd-containing sample has a higher zero-field resistivity. For x = 0.2, a peak is shown in both ρ and MR_H near T_C. Zero-field ρ reveals semiconductor-like behavior at temperatures for both $T > T_C$ and T far below T_C, which is similar to the results of $FeCr_2S_4$. Upon substitution of Cd for Fe, both the zero-field ρ and MR_H value increases monotonically, while the peak of the MR_H

curve shifts to lower temperatures. As mentioned above, it is believed that the conduction originates from Fe^{2+} narrow band at temperatures far below T_C, and is dominated by the magnetic polarons in the temperature region above T_C. For $Fe_{1-x}Cd_xCr_2S_4$, there are two sided influences of the introduced Cd^{2+} on the conduction behavior. On the one hand, since the conduction originates from Fe^{2+} narrow band, the increase of Cd ions will decrease carrier density, resulting in the increase of ρ. As is mentioned above, the magnetic polaron hopping conduction $\rho = \rho_0 T \exp(E/k_BT)$ should be considered for $T > T_C$. On the other hand, the introduced Cd ions will induce both Coulomb and magnetic potential fluctuations, as a sequence, leading to the formation of a mobility edge. Thus, thermally activated behavior $\rho = \rho_0 \exp(E/k_BT)$ due to a mobility edge may be more appropriate to describe the conduction above T_C [32, 33].

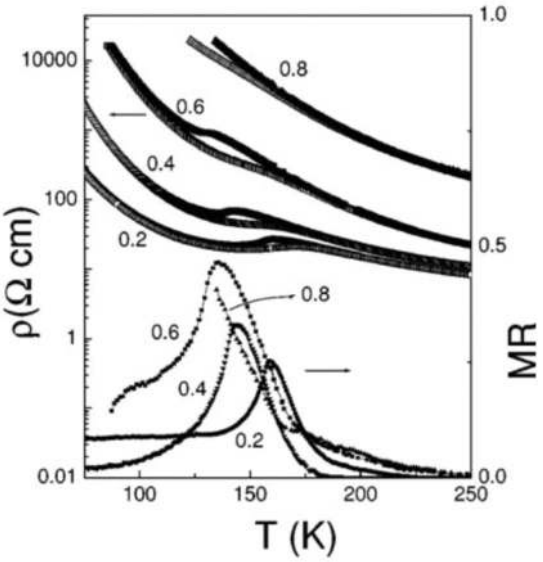

Figure 4. Resistivity ρ and magnetoresistance $MR_H = [\rho(0) - \rho(H)]/\rho(0)$, versus temperature for $Fe_{1-x}Cd_xCr_2S_4$ ($0 < x \leq 0.8$) [31].

Figure 5 shows the zero-field resistivity curves replotted as $\ln \rho - 1000/T$ and $\ln(\rho/T) - 1000/T$, respectively. For $x = 0.2$, the curve of $\ln \rho - 1000/T$ is linear both at $T > T_C$ and at temperatures far below T_C. The activation energy E, which is obtained from the fits to $\rho = \rho_0 \exp(E/k_BT)$, is 39 meV for the temperatures far below T_C, and 50 meV for $T > T_C$. As is known, the discrepancy of the activation energy for $FeCr_2S_4$ is described by a two-fluid model concerning the coexistence of magnetic polarons and naked carriers. As is shown in **Figure 5(a)**, magnetic polaron hopping conduction [$\rho = \rho_0 T \exp(E/k_BT)$] is more appropriate for the resistivity behavior at $T > T_C$. Moreover, it gives more convincible description as compared to thermal-activated mechanism for higher Cd concentration, which implies that the magnetic polarons may be more stable in the high-Cd samples.

http://dx.doi.org/10.5772/110953

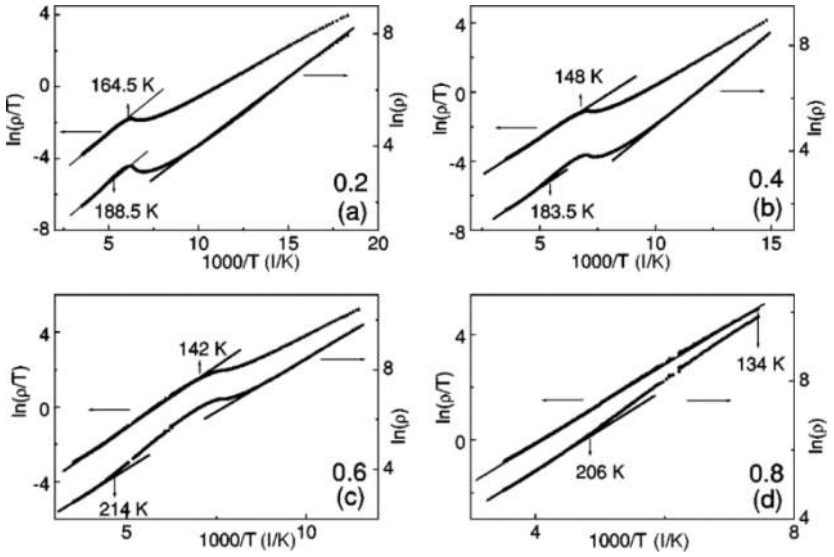

Figure 5. Zero-field resistivity curves for $Fe_{1-x}Cd_xCr_2S_4$ ($0 < x \leq 0.8$) replotted as ln ρ − 1000/T (closed circle ●) and l ln(ρ/T) − 1000/T (solid square ■), respectively [31].

Direct evidence of the magnetic polarons could be best sought with electron spin-resonance spectroscopy (ESR) measurements [31]. Above T^* ~ 113 K, each spectrum consists of a single line with a Lorentzian line shape, and further decreasing temperature, some distortions occur. A similar behavior has been observed in manganese perovskites, which is attributed to the presence of the FM clusters embedded in PM matrix [34, 35]. In addition, as T is increased, the peak-to-peak line-width ΔH_{PP} decreases in a broad temperature range [31]. T_{min} (corresponding to the temperature where ΔH_{PP} is minimum) is much higher than T^*, suggesting that the relaxation mechanism dominating in $CdCr_2S_4$ is different with that in the manganese. The analysis of ESR experiments in CMR materials has pointed out that line-width ΔH_{PP} will decrease exponentially upon warming if the magnetic polaron acts as a part in the relaxation mechanism, as a result of the motionally narrowed relaxation mechanism [36]. Thus in $CdCr_2S_4$, since magnetic polaron is more stable upon Cd substitution, it is plausible that the hopping of magnetic polarons will make contribution to the relaxation process, and certainly decrease the line-width ΔH_{PP}. The decrease of line-width with increasing temperature obviously gives a direct evidence for the presence of magnetic polarons in $CdCr_2S_4$.

For a pure magnetic polaron system, the magnetic polaron forms by self-trapping in a ferromagnetically aligned cluster of spins at $T < T_P$ (T_P denotes the temperature where polarons start forming). As the temperature is lowered toward T_C, the polaron grows in size. According to the ML model [37], for a low carrier density ferromagnet, when $n\xi \approx 1$ is accomplished, magnetic polarons overlap, which leads to the carrier delocalization. Here n is the carrier

density, andξ is FM correlation length. It provides the temperature ratio of about $T/T_C \leq 1.05$–1.1 [37]. Therefore, for a pure magnetic polaron system, the magnetic polarons are periodically spaced before overlapping, similar to a gas of magnetic polarons. When the system is in a PM state, no magnetic correlation occurs among the polarons to be considered as superparamagnetic. On the other hand, if the system is inhomogeneous, there may be magnetic correlation, which means magnetic polarons themselves are no longer isolated. Due to the correlation, the system could not stay in the superparamagnetic state, which results in the existence of some distortions in the resonance line [34]. Hence, it can be concluded that magnetic polarons first exist as a gas of polarons at temperatures $T < T_P$, and then transform into correlated polarons at temperatures $T < T^*$ ($T_P > T^* > T_C$).

4. Colossal magnetocapacitance in $CdCr_2S_4$

Multiferroic materials that exhibit simultaneous magnetic and ferroelectric order as well as concomitant magnetoelectric coupling have attracted special interest in recent years [38–40]. $CdCr_2S_4$ was originally investigated as a FM semiconductor more than 40 years ago [41]. Recently, it was reported that SC $CdCr_2S_4$ exhibits multiferroic behavior with the evidence of relaxor ferroelectricity and CMC [6]. Soon after, similar magnetoelectric effect has also been revealed in other related thio-spinel compounds, that is, $CdCr_2Se_4$ and $HgCr_2S_4$ [42, 43]. However, the emergence of ferroelectricity and CMC effect in these thio-spinels was found to be highly sensitive to the detail of sample preparation and chemical doping. Annealing SC samples in vacuum or sulfur atmosphere led to a suppression of relaxation features, and no remanent electric polarization could be found at low temperatures [14]. In addition, multiferroicity and CMC effect are absent in undoped PC samples, but present in indium-doped PCs [14]. Accordingly, the question of whether the magnetoelectric effect in $CdCr_2S_4$ is intrinsic or not has been raised [44, 45]. In this section, the origin of CMC effect in the $CdCr_2S_4$system would be revealed systematically through the magnetic, dielectric and electric transport measurements of $CdCr_2S_4$ and $Cd_{0.97}In_{0.03}Cr_2S_4$ PC samples before and after annealing in cadmium vapor.

Upon doping and annealing, no impurity phases are detected [46]. The *M-T* curves under an external magnetic field of 1 T for all samples are shown in the inset of **Figures 6(b)** and **7(b)**. After annealing in cadmium vapor, the magnetic properties of PC $CdCr_2S_4$ and $Cd_{0.97}In_{0.03}Cr_2S_4$ are slightly changed. The Curie temperature T_C is about 92.1 K for $CdCr_2S_4$ and 92.9 K for $Cd_{0.97}In_{0.03}Cr_2S_4$, respectively. After annealing, the increase of T_C is less than 4 K. **Figures 6** and **7** display the temperature dependence of dielectric constant ε' and *ac*-conductivity σ'at two different frequencies in magnetic field of 0 T and 4.5 T for the as-prepared and annealed samples. Both ε' and σ' increase with temperature monotonously and do not show anomaly and magnetic field dependence in the whole measured temperature range, as seen from **Figures 6(a**, **b)** and **7(a**, **b)**. After annealing $CdCr_2S_4$ at 800°C (**Figure 6(c**, **d)**), ε' displays a hump in the low temperature region and the hump temperature increases with frequency, implying a relaxor-like behavior of the dielectric property [14]. However, the magnetic field of 4.5 T still has no obvious effect on either ε' or σ'.

http://dx.doi.org/10.5772/110953

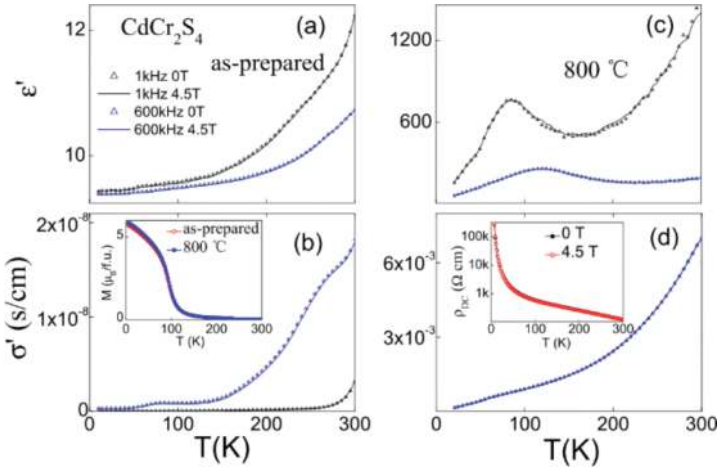

Figure 6. Temperature dependence of dielectric constant (upper frames) and *ac*-conductivity (lower frames) for the as-prepared and annealed $CdCr_2S_4$ samples. Inset of (b) and (d) show temperature dependence of magnetization and resistivity in magnetic field of 0 and 4.5 T for annealed $CdCr_2S_4$, respectively [46].

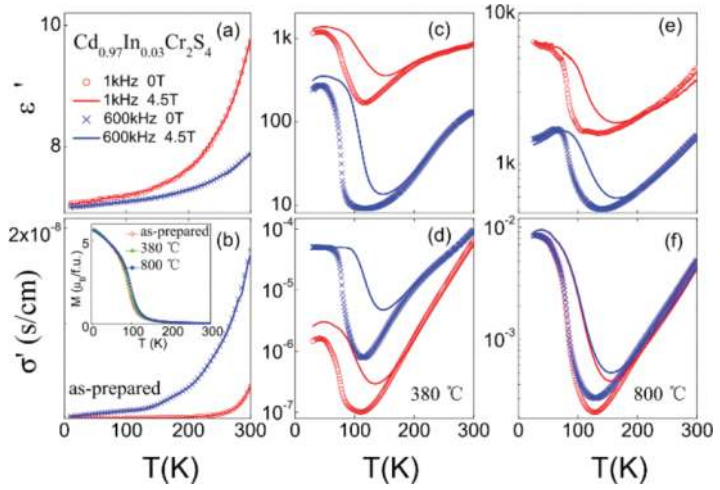

Figure 7. Temperature dependence of dielectric constant (upper frames) and *ac*-conductivity (lower frames) for the as-prepared and annealed $Cd_{0.97}In_{0.03}Cr_2S_4$ samples. Inset of (b) shows the temperature dependence of magnetization [46].

In contrast, for the $Cd_{0.97}In_{0.03}Cr_2S_4$ sample annealed at 380°C (**Figure 7(c, d)**), a strong upturn of ε' is clearly observed with decreasing temperature near T_C. σ' has a similar temperature dependence as ε'. The external magnetic field of 4.5 T does not change the shape of ε'-T and σ'-T curves, but makes the upturn of ε' and σ' shifting toward higher temperatures. Magnetocapacitance, defined as MC = (ε'(4.5 T) − ε'(0 T))/ε'(0 T), reaches up to 290% at 1 kHz and

1950% at 600 kHz (**Figure 8(a)**). The sample annealed at 800°C has similar temperature dependence of ε' and σ' as the sample annealed at 380°C, while has a much higher ε' and σ', and a lower MC value (reaches up to 145% at 1 kHz and 104% at 600 kHz, see **Figure 8(c)**). A clear feature in **Figures 6(c**, **d)**, and **7(c**, **f)** is that the appearance of CMC effect is accompanied by the field-enhanced ac conductivity. The inset of **Figure 6(d)** shows the temperature dependence of DC-resistivity under 0 T and 4.5 T for the annealed $CdCr_2S_4$ sample. In accordance with the field independence of the *ac*-conductivity, the application of 4.5 T magnetic field has no evident influence on the DC-resistivity. Upon cooling, the DC-resistivity increases monotonously as a typical semiconductor behavior in the whole temperature range measured. However, as seen in **Figure 8(b**, **d)**, the temperature dependence of DC-resistivity for the annealed $Cd_{0.97}In_{0.03}Cr_2S_4$ samples is quite different from that of $CdCr_2S_4$. For annealed $Cd_{0.97}In_{0.03}Cr_2S_4$, the zero-field resistivity first increases with decreasing temperature. After reaching up to a maximum near T_C, the resistivity decreases abruptly, indicating the occurrence of insulator-metal transition. Upon further cooling to the low temperature region, the resistivity increases again. Being correlated to the insulator-metal transition around T_C, the external magnetic field of 4.5 T makes the resistivity peak moving to a higher temperature and dramatically depresses the peak value. Magnetoresistance, defined as MR = (ρ(0 T) − ρ(4.5 T))/ρ(0 T), reaches up to about 95% for the sample annealed at 380°C and 93% for the sample annealed at 800°C, much higher than the value of the most-investigated CMR material $FeCr_2S_4$, see the insets of **Figure 8(b**, **d)** [5, 31].

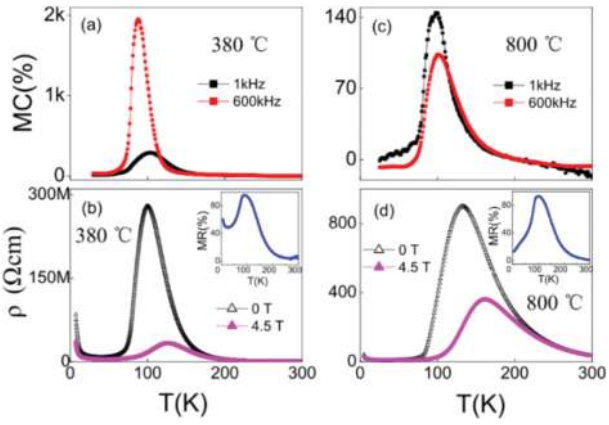

Figure 8. Temperature dependence of magnetocapacitance (upper frames) and resistivity (lower frames) for annealed $Cd_{0.97}In_{0.03}Cr_2S_4$. Insets of (b) and (d) display the magnetoresistance of the samples annealed at 380°C (left) and 800°C (right), respectively [46].

The appearance of CMC in the $CdCr_2S_4$ system is always accompanied by CMR. To confirm that the CMC can be described by a combination of CMR and Maxwell-Wagner effects, the impedance spectroscopy of $Cd_{0.97}In_{0.03}Cr_2S_4$ annealed at 380°C is fitted to a Maxwell-Wagner equivalent circuit. The impedance spectroscopy is converted from capacitance and dielectric loss tangent in the frequency range from 100 Hz to 600 kHz. The circuit consists of two

subcircuits in series, each containing a resistor (R) and a capacitor (C) in parallel, as depicted in the inset of **Figure 9(a)**. Z is better described by using the Cole-Cole equation: $Z = R/(1+(i\omega RC)^n)$, $(0 \le n \le 1)$ [47, 48]. The fitting was performed with all parameters unlocked. Take the data under zero magnetic field for the $Cd_{0.97}In_{0.03}Cr_2S_4$ sample annealed at 380°C for example. The impedance spectroscopy can be fitted well in the temperature range from 79 K to 189 K, see the solid lines in **Figure 9(a)**. The temperature-dependent total resistance $R_1 + R_2$ derived from the fitting coincides with the temperature dependence of the measured DC resistance, as shown in **Figure 9(b)**.

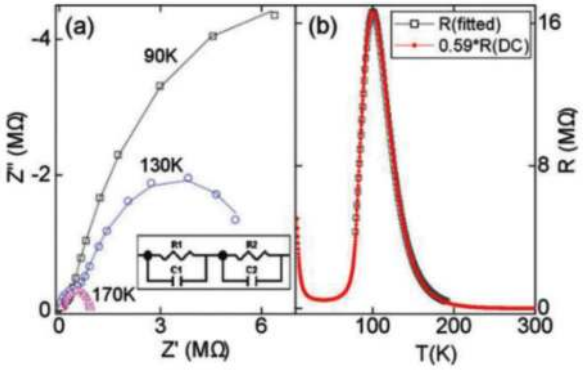

Figure 9. (a) The complex impedance plot at 90, 130 and 170 K for the $Cd_{0.97}In_{0.03}Cr_2S_4$ sample annealed at 380°C. The solid line is the fitting result based on the equivalent circuit displayed in the inset. (b) Temperature dependence of the fitted resistance and measured DC resistance (multiplied by 0.59) [49].

The perfect match between the resistance derived from the impedance spectroscopy and the DC resistance strongly suggests that the annealed $Cd_{0.97}In_{0.03}Cr_2S_4$sample contains two components with different electrical response. These two components can be a sample and an electrode, or a grain and a grain boundary. In these cases, an applied bias voltage can change the capacitance and the ac conductance [50–52]. Moreover, Hemberger et al. have experimentally excluded any electrode effects on the magnetodielectric response and excluded any nonhomogeneous impurity distribution in their SC $CdCr_2S_4$ [42, 45]. Thus, CMC effect could not be attributed to the extrinsic Maxwell-Wagner effect. In phase-separated manganite, strong magnetodielectric effect is resulted from the scenario of phase separation [53–56]. The thermoelectric-power and ESR measurements reveal the existence of magnetic polarons in the annealed $Cd_{0.97}In_{0.03}Cr_2S_4$ sample [49]. As is discussed in the above section, magnetic polaron is similar as the presence of the FM clusters embedded in PM matrix, indeed a kind of phase separation in nature [24, 57, 58]. For the exchange interaction with localized spins, the energy of the conduction electron in the FM cluster is smaller than that in the PM host, which results in a nanoscale charge and phase separation [57, 58]. Upon cooling, magnetic polarons grow in size, as a consequence, their overlap induces larger metallic clusters and finally a percolative metallic filament. After the insulator-metal transition, the coexistence of FM metallic and PM insulating phases is replaced by a complete FM order founded in all the regions. The interfacial

polarization or space-charge yielded by the mixture of insulating and metallic regions would cause a dielectric response, which is intrinsic to the material. Therefore, the dielectric response can be attributed to a combination of magnetoresistance and an intrinsic Maxwell-Wagner effect, as observed in the phase-separated manganite [53–56].

5. Negative thermal expansion in $ZnCr_2Se_4$

Recently, $ZnCr_2Se_4$ has been observed to display NTE and a large magnetostriction [2]. To study the very origin of NTE, a set of experimental techniques is utilized to probe the spin-lattice correlation in $ZnCr_2Se_4$. **Figure 10(a)** shows the temperature dependence of lattice constant a. With decreasing temperature, a first decreases rapidly and then manifests a NTE behavior below about T_E = 60 K. Upon further cooling below 20 K, splitting of several peaks in XRD spectra is observed. **Figure 10(b)** presents the magnetization versus T at low-applied magnetic field of 100 Oe. A fitting of the inverse susceptibility $1/\chi$ according to the PM Curie-Weiss (CW) law $1/\chi = (T - \Theta_{CW0})/C$ is shown in **Figure 10(c)**. A large positive CW temperature Θ_{CW0} = 85 K and the coefficient C = 3.74 are obtained. The large positive CW temperature implies a dominant FM exchange interaction; however, the compound shows an AFM ordering at low temperatures. On the other hand, both the constant g-factor and linear behavior of peak-to-peak linewidth (ΔH_{PP}) in the ESR spectrum evidence a well-defined PM state at least above 100 K [59]. Thus, the inverse susceptibility should be described by the PM CW law down to this temperature. However, it departs from the linear behavior at a temperature as high as about 180 K, see **Figure 10(c)**. Recalling the fitting process in **Figure 10(c)**, a constant CW temperature Θ_{CW0} has been assumed, that is, a constant magnetic exchange interaction J. In addition, the nearest neighbor FM Cr-Se-Cr and other neighbor AFM Cr-Se-Zn-Se-Cr super-exchange interactions depend strongly on the lattice constant [1]. It means that the total J may change since a decreases dramatically upon cooling. Accordingly, the traditional CW behavior should be modified within the present case. In specific, one should take a variable Θ_{CW} (or J) as a function of T or a into account.

In AFM spinel oxides, the CW temperature changes exponentially with the lattice parameter [60]. Naturally, an empirical description of $\Theta_{CW}(T) = \Theta_{CW0} - \Theta^* e^{-T/\beta}$ is postulated. The fitting of the inverse susceptibility above 100 K using the modified CW behavior $1/\chi = (T - \Theta_{CW}(T))/C$ is exhibited in **Figure 11(a)**. The parameters are Θ = 226 and β = 45. Furthermore, a remarkable deviation below 100 K in blue short-dashed line indicates the appearance of the effective internal field originating from FM clusters. Next, based on the obtained Θ and β, Θ_{CW}(T) is extrapolated to low temperatures as exhibited in **Figure 11(b)**. It shows a derivation at about 180 K from the nearly constant value. With further lowering temperature, it decreases faster and faster and below $T \approx 45$ K, Θ_{CW}(T) even becomes negative. These features may interpret qualitatively the fact that $ZnCr_2Se_4$ is dominated by ferromagnetic exchange interaction but orders at low temperatures antiferromagnetically. Since the exchange integral and the CW temperature are linked by $J(T) \propto \Theta_{CW}$(T) [$J(a) \propto \Theta_{CW}(a)$], we will use $J(T)$ [$J(a)$] instead in the following discussion. Given that J is changeable, magnetic exchange and lattice elastic energies can link

effectively with each other via magnetoelastic coupling. The free energy F in a magnetoelastic system is expressed as:

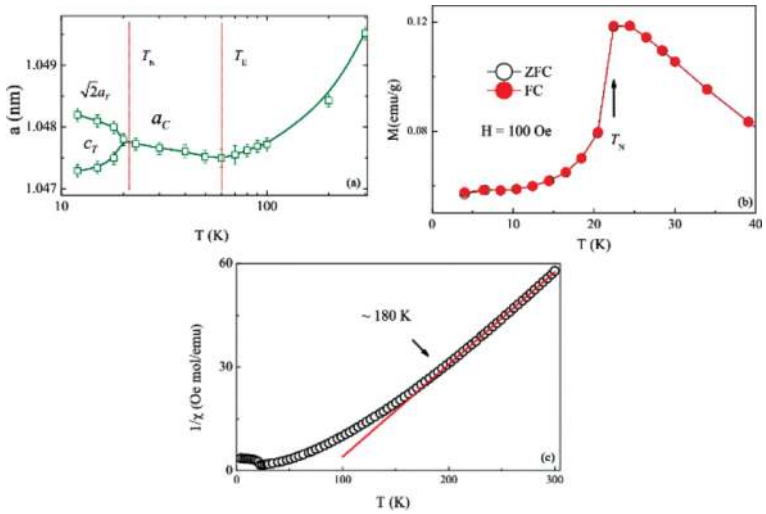

Figure 10. (a) Temperature dependent lattice parameter a versus T for $ZnCr_2Se_4$. (b) Low temperature dependence of the magnetization M at 100 Oe. (c) A Curie-Weiss fitting of the inverse susceptibility [59].

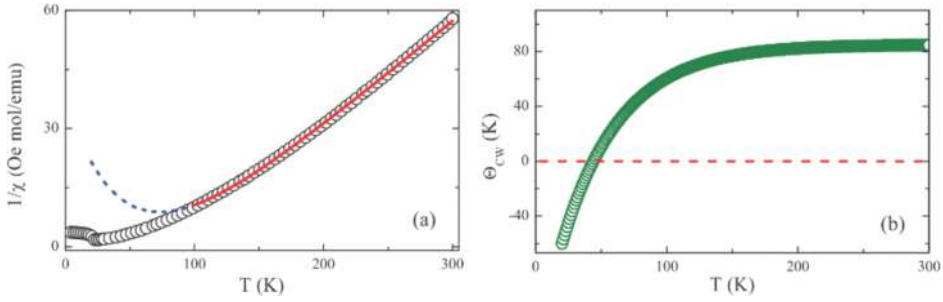

Figure 11. (a) A fitting of the inverse susceptibility above 100 K in red solid line using $1/\chi = (T - \Theta_{CW}(T))/C$ taking a temperature or lattice constant a dependent CW temperature into account. The short-dashed blue line is an extension of the fitting to low temperatures. (b) Θ_{CW} versus T and the red dashed line indicates $\Theta_{CW} = 0$ at 45 K [59].

$$F(T) = -J(T)\sum_{ij}\overrightarrow{S_i}\cdot\overrightarrow{S_j} + \frac{1}{2}N\omega^2\Delta^2(T) - T\cdot S(T) \tag{2}$$

where N is the number of the ion sites, ω is the averaged vibrational angular frequency, and Δ is the averaged strain relative to the equilibrium lattice constant. The first term is exchange

energy (E_{ex}) as a function of J, the second is lattice elastic energy (E_{el}) related mainly to the lattice parameter a (or equivalent T), and the last is the entropy. From the above equation, if the system stays at an ideal PM state, then $E_{ex} = 0$. So E_{ex} and E_{el} will show no coupling.

When the system stays in FM state with a changeable J, there may exist a competition between E_{ex} and E_{el} since the former is negative while the latter always is positive. Indeed, it has been concluded above that J decreases exponentially [**Figure 11(a)**] and some FM clusters form gradually below 100 K. Therefore, the concomitant decrease of J and a causes an increasing E_{ex} but decreasing E_{el} in the FM clusters. At some critical point, a totally compensation between them may present. If a further decreases upon cooling, the variation of E_{ex} would gradually exceed that of E_{el} in magnitude. Especially when J drops sharply with respect to a, say here at T_E, a tiny decrement of a will give rise to a dramatic increment of E_{ex}, whereas E_{el} keeps nearly constant. The state in a system subjected to stimuli, such as cooling, always tends to develop toward one that can lower F. In this sense, it is favorable to lowering F by expanding the lattice parameter a to increase J ($J > 0$), and thereby to decrease E_{ex} due to its negative value, at the same time at a cost of small increases of E_{el} in magnitude. This means that a NTE of the lattice originating from the FM clusters with an exponentially changeable J is expected. It is noted that when applying a magnetic field to the system in the NTE temperature region, magnitude of NTE enhances [2]. This is because the size or population of the FM clusters increases when applying a magnetic field. On the contrary, when an AFM ordering appears, J becomes negative and the condition to stimulate NTE is not met any more. Normal thermal expansion upon cooling results in a simultaneous decreasing of E_{ex} and E_{el}, which is consistent to lowering F. In fact, a normal expansion feature is observed below T_N [2]. It should be noted that the existence of NTE evidences in turn that J is changeable [2, 61]. If J keeps constant in a FM cluster, E_{ex} will be almost constant and a normal thermal expansion of the lattice alone can give rise to a decrease of E_{el} and of F sufficiently.

The thermal expansion data for $ZnCr_2(Se_{1-x}S_x)_4$ ($0 \le x \le 0.1$) SC samples is represented as the function of $\delta = [L(T) - L_0]/L_0$ from 4 K to 300 K in **Figure 12(a)**, where L_0 is the length of the sample at room temperature. For $ZnCr_2Se_4$, as T is lowered, δ first decreases monotonically and reaches a minimum at $T_m \sim 50$ K. Then δ begins to increase, followed by a steep downturn upon further cooling across T_N. For the S-doped samples, the striction below T_N becomes gentler, while the temperature region of the NTE is expanded. As seen from the inset of **Figure 12(a)**, T_N moves to lower temperatures with increasing S content while T_m shifts oppositely. To further probe the nature of spin-lattice coupling in the complex magnetic state, the field dependence of both magnetization and magnetostriction δ at 5 K for all the $ZnCr_2(Se_{1-x}S_x)_4$ ($0 \le x \le 0.1$) samples are illustrated in **Figure 12(b, c)**. δ is defined as $\delta = [L(H) - L(0)]/L(0)$, and $L(0)$ is the length of the sample at zero field. Due to strong spin-lattice coupling, a one-to-one correlation between M-H and δ-H is clearly reflected in **Figure 12(b, c)**. At both of the characteristic fields of H_{C1} and H_{C2}, δ also displays an anomaly. Being associated to domain reorientation, hysteresis is also observed below H_{C1} as the magnetic field returns to zero, see **Figure 12(b, c)**. For $x = 0.05$ and 0.10, field dependence of magnetization is still inconsistent with the magnetostriction data. With increasing S content, the hysteresis behavior below H_{C1} wanes in both M-H and δ-H, and completely vanishes at $x =$

0.10 [9]. In addition, the magnetization and magnetostriction data are both suppressed by an order of magnitude.

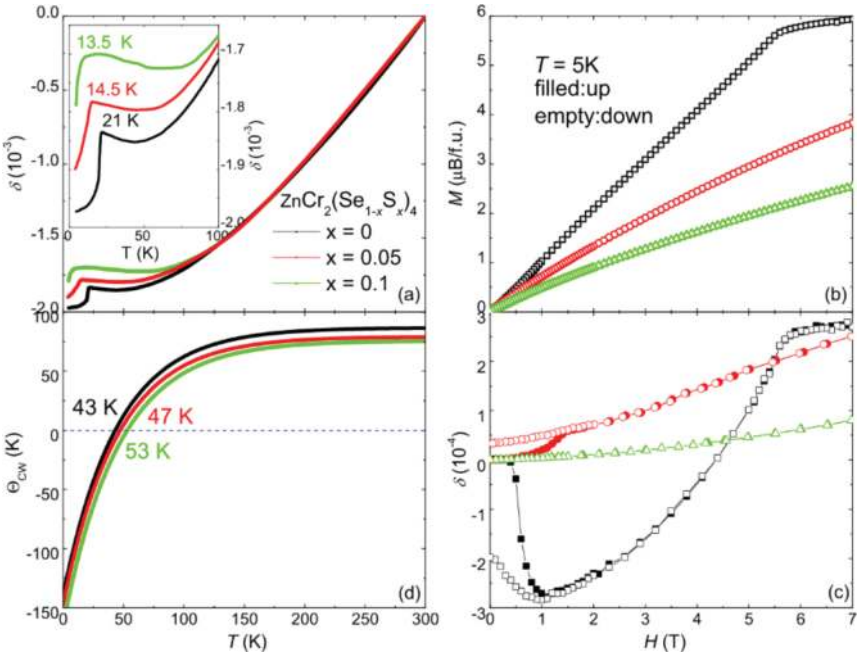

Figure 12. (a) The thermal expansion plotted as $\delta = [L(T) - L_0]/L_0$ for SC $ZnCr_2(Se_{1-x}S_x)_4$ ($0 \le x \le 0.1$) from 5 K to 300 K, where L_0 is the length of the sample in a paramagnetic state at 300 K. The inset shows the enlarged view of the low-temperature region. (b) Magnetic field dependence of magnetization; (c) Magnetostriction plotted as $\delta = [L(H) - L(0)]/L(0)$ at 5 K for SC $ZnCr_2(Se_{1-x}S_x)_4$ ($0 \le x \le 0.1$), where $L(0)$ is the length of each $ZnCr_2(Se_{1-x}S_x)_4$ ($0 \le x \le 0.1$) sample at zero field. (d) The variable CW temperature plotted as $\Theta_{CW}(T)$ versus T [9].

To investigate the NTE and magnetostriction in S-substituted samples, the inverse susceptibility was analyzed by the same method as is proposed above, which is shown in **Figure 12(d)** [59]. For $ZnCr_2Se_4$, $\Theta_{CW}(T)$ drops dramatically and changes sign at 43 K, close to the onset temperature of NTE. The substitution of S for Se drives Θ_{CW0} to lower temperature on account of an enhancement of the AFM exchange interaction, while the temperature corresponding to the sign change in $\Theta_{CW}(T)$ is increased. It could explain why the temperature region of the NTE is extended in $ZnCr_2(Se_{1-x}S_x)_4$ ($0 < x \le 0.1$) samples. The substitution of sulfur for selenium not only enhances the AFM exchange interaction, but also leads to a Cr-Cr bond disorder [9]. The bond disorder frustrates the spins and finally leads to a spin-glass state. In a spin-glass state, since the spin arranges or freezes randomly upon cooling to lower temperature, the magnetic exchange and lattice elastic energy are decoupled. Note that, in the S-substituted samples, potential striction or shrinkage of the lattice can still be observed upon cooling across T_N, which implies that a partial long-range AFM ordering still manifests and coexists with the spin-glass state.

6. Complex orbital states in spinel $FeCr_2S_4$

Due to strong frustration, the spinel $FeCr_2S_4$ not only shows the fascinating CMR effect, but also displays complex orbital states [12, 13]. Recently, it was reported to display the orbital glass state in SC samples, while it displays orbital ordering in PC ones [12, 13]. In $FeCr_2S_4$, the Fe^{2+} ion is tetrahedrally coordinated by the sulfur ions, with an electronic configuration $e_g^3 t_{2g}^3$ and $S = 2$, is a typical JT active. Thus, it might induce long-range orbital order at low temperatures [62, 63]. In addition, the diamond lattice formed by Fe ions is geometrically frustrated for the orbital degrees of freedom [12, 13]. Thus, Fichtl et al. proposed two possible explanations to interpret the discrepancy of different orbital states in $FeCr_2S_4$ [12]. One is that the orbital glass state is attributed to geometric frustration in the SC, and broken in the PC by marginal disorder. Alternatively, the orbital ordering in the SC is suppressed by small disorder (such as chlorine defects from the growth process). To verify the role of disorder in these two possibilities, the physical properties of some SC and doped PC $FeCr_2S_4$ are presented in detail next.

Figures 13(a) and **14** display the magnetization as a function of temperature obtained in ZFC and FC processes with $H = 0.005$ T. All samples display clear anomalies around 65–75 K and irreversibility between ZFC and FC curves. The cusp-like anomaly was early correlated to an abrupt increase of magnetic anisotropy below $T_m \sim 70$ K, and recently attributed to a spin-reorientation transition associated with the onset of short-range orbital ordering [64, 65]. Moreover, the PC $FeCr_2S_4$ displays a step-like anomaly in the magnetization around $T_{OO} \sim 9$ K in **Figure13(a)**. For the other samples, the transition is replaced by a smooth temperature dependence, which is shown in the insets of **Figure 14**. The step-like anomaly for PC and smooth temperature dependence for other ones can be related to the orbital-ordering (OO) transition and orbital glass state, respectively [66]. A similar temperature-dependent magnetization between SC and doped PC samples suggests that the orbital order might also be frozen in these samples. Temperature dependence of specific heat for PC $FeCr_2S_4$ is shown in **Figure 13(b)**. It displays a well-defined λ-type anomaly around 9 K, indicative of the OO transition, which is consistent with the step-like transition in magnetization [12, 13]. For the other samples, the λ-type anomaly is entirely inhibited and becomes a broad hump, see **Figure 14(e)**. In addition, as T is lowered below 2 K, the heat capacity approaches zero following a strict T^2-dependence in the insets of **Figure 14(e)**. In contrast, the specific heat of PC deviates from the linear behavior in low temperatures below 2 K, shown in the inset of **Figure 13(b)**. The earlier reports pointed out that the phonon and magnon contribution to the specific heat of SC could be ignorable as compared to the orbital contribution at ultra-low temperatures [12, 13]. Thus, the existence of the orbital glass state in both SC and doped samples is plausible, since heat capacity of orbital order suppressed by random fields obeys the T^2-dependence predicted by the theoretical calculation [67]. Clearly, all the results reveal that the orbital moment has been frozen into the orbital glass state in the SC and doped PC samples.

For a different orbital state, the orientation of the orbital is coupled to the elastic response of the ionic lattice via electron-phonon interaction, and therefore a different orbital state is accompanied by a different charge distribution [68]. The resistivity curves in the function of $\ln \rho$-$1000/T$ and $\ln \rho$-$(1000/T)^{1/4}$ are shown in **Figures 13(c)** and **15**, respectively. The conduction

mechanism for PC $FeCr_2S_4$ has been studied in detail in the previous section. In the low temperatures below 37 K, the resistivity could be better described by a semiconductor-like behavior. Upon warming, a curvature emerges, which might be related to the formation of short-range orbital order state [12]. For the other samples, the Mott's variable-range hopping is more appropriate to fit the feature of resistivity. As we know, for variable-range hopping, it is necessary that the system exists random potential fluctuations, being related to the degrees of disorder [32]. Hence, the presence of random potential could be the reason for the emergence of orbital glass state [12, 13].

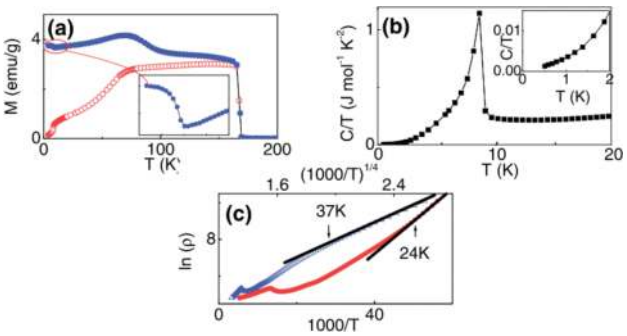

Figure 13. (a) Temperature dependence of ZFC (red circle) and FC (blue circle) magnetization in H = 0.005 T for PC $FeCr_2S_4$. The inset shows an enlarged view at low temperatures. (b) The specific heat plotted as C_P/T versus T for PC $FeCr_2S_4$. The inset shows an enlarged view at temperatures below 2 K. (c) Resistivity curves in the function of ln ρ – 1000/T (blue triangle) and ln ρ-(1000/T)$^{1/4}$ (red circle) for PC $FeCr_2S_4$. The solid lines are a guide to eyes [10].

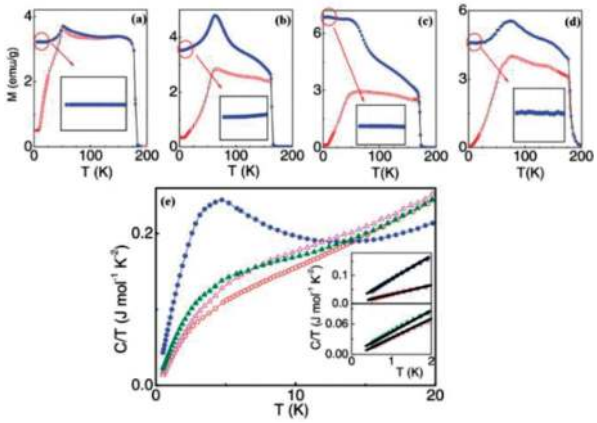

Figure 14. Temperature dependence of magnetization at 0.005 T for (a) SC $FeCr_2S_4$, (b) $FeCr_{1.9}Al_{0.1}S_4$, (c) $FeCr_{1.95}Ga_{0.05}S_4$ and (d) $Fe_{1.05}Cr_{1.95}S_4$. The insets show enlarged views of the magnetization at low temperatures. (e) The specific heat in the function of C_P/T versus T for SC $FeCr_2S_4$ (red circle), $FeCr_{1.9}Al_{0.1}S_4$ (blue circle), $FeCr_{1.95}Ga_{0.05}S_4$ (violet triangle) and $Fe_{1.05}Cr_{1.95}S_4$ (olive triangle). The insets show enlarged views below 2 K. The solid lines are a guide to eyes [10].

In conclusion, complex orbital states in $FeCr_2S_4$ are driven by the coexistence of strong electron-phonon coupling and geometrical frustration. The different orbital states in PC and SC $FeCr_2S_4$ reveal the exquisite balance between frustration and strong coupling among different degrees of freedom. The magnetism, heat capacity and resistivity properties of all the samples give clear evidence that the disorder in SC and doped samples raises random potential up, freezes the orbital order and finally results in orbital glass state.

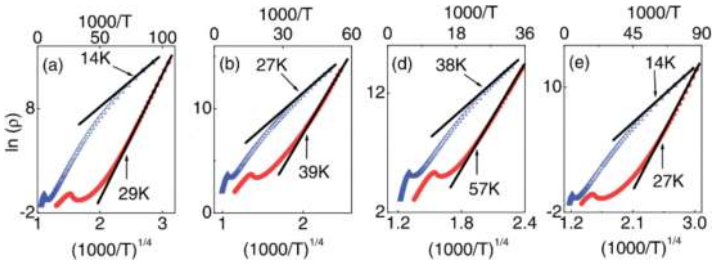

Figure 15. Resistivity curves in the function of ln ρ − 1000/T (blue triangle) and ln ρ − (1000/T)$^{1/4}$ (red circle) for (a) SC $FeCr_2S_4$, (b) $FeCr_{1.9}Al_{0.1}S_4$, (c) $FeCr_{1.95}Ga_{0.05}S_4$ and (d) $Fe_{1.05}Cr_{1.95}S_4$. The solid lines are a guide to eyes [10].

7. Conclusion

Due to the presence of frustration as well as strong coupling among spin, charge, orbital and lattice degrees of freedom, Cr-based chalcogenide spinels display rich physical effects and complex ground states. There is still some open questions such as the nature of spin nematic, correlation between orbital state and magnetic structure, which should be addressed in future under the conditions of high pressures and high magnetic fields.

Acknowledgements

This work is financially supported by the National Natural Science Foundation of China under Grant nos. U1332143 and 11574323.

Author details

Chuan-Chuan Gu, Xu-Liang Chen and Zhao-Rong Yang*

*Address all correspondence to: zryang@issp.ac.cn

High Magnetic Field Laboratory, Chinese Academy of Sciences, Hefei, China

http://dx.doi.org/10.5772/110953

References

[1] P. K. Baltzer, P. J. Wojtowicz, M. Robbins and E. Lopatin, *Phys. Rev*. 151, 367 (1966).

[2] J. Hemberger, H.-A. K. v. Nidda, V. Tsurkan and A. Loidl, *Phys. Rev. Lett*. 98, 147203 (2007).

[3] L. Q. Yan, J. Shen, Y. X. Li, F. W. Wang, Z. W. Jiang, F. X. Hu et al., *Appl. Phys. Lett*. 90, 262502 (2007).

[4] I. Kim, Y. S. Oh, Y. Liu, S. H. Chun, J.-S. Lee, K.-T. Ko et al., *Appl. Phys. Lett*. 94, 042505 (2009).

[5] A. P. Ramirez, R. J. Cava and J. Krajewski, *Nature* 386, 156 (1997).

[6] J. Hemberger, P. Lunkenheimer, R. Fichtl, H.-A. K. v. Nidda, V. Tsurkan and A. Loidl, *Nature* 434, 364 (2005).

[7] K. Ohgushi, T. Ogasawara, Y. Okimoto, S. Miyasaka and Y. Tokura, *Phys. Rev. B* 72, 155114 (2005).

[8] K. Siratori and E. Kita, J. Phys. Soc. Jpn. 48, 1443 (1980).

[9] C. C. Gu, Z. R. Yang, X. L. Chen, L. Pi and Y. H. Zhang, *J. Phys. Conden. Matt*. 28, 18LT01 (2016).

[10] R. Tong, Z. R. Yang, C. Shen, X. B. Zhu, Y. P. Sun, L. Li et al., *EPL* (Europhysics Letters) 89, 57002 (2010).

[11] V. Felea, S. Yasin, A. Günther, J. Deisenhofer, H.-A. Krug von Nidda, S. Zherlitsyn et al., *Phys. Rev. B* 86, 104420 (2012).

[12] R. Ficht, V. Tsurkan, P. Lunkenheimer, J. Hemberger, V. Fritsch, H.-A. Krug von Nidda et al., *Phys. Rev. Lett*. 94, 027601 (2005).

[13] N. Büttgen, J. Hemberger, V. Fritsch, A. Krimmel, M. Mücksch, H.-A. K. v. Nidda et al., *New J. Phys*. 6, 191 (2004).

[14] J. Hemberger, P. Lunkenheimer, R. Fichtl, S. Weber, V. Tsurkan and A. Loidl, *Phase Transit*. 79, 1065 (2006).

[15] Z. R. Yang, S. Tan and Y. H. Zhang, *Phys. Rev. B* 64, 024401 (2001).

[16] Z. R. Yang, S. Tan and Y. H. Zhang, *Phys. Rev. B* 65, 184404 (2002).

[17] S.-H. Lee, C. Broholm, W. Ratcliff, G. Gasparovic, Q. Huang, T. H. Kim et al., *Nature* 418, 856 (2002).

[18] S.-H. Lee, C. Broholm, T. H. Kim, W. Ratcliff II and S.-W. Cheong, *Phys. Rev. Lett*. 84, 3718 (2000).

[19] M. McCormack, S. Jin, T. H. Tiefel, R. M. Fleming, J. M. Phillips and R. Ramesh, *Appl. Phys. Lett*. 64, 3045 (1994).

[20] S. Jin, T. H. Tiefel, M. McCormack, R. A. Fastnacht, R. Ramesh and L. H. Chen, *Science* 264, 413 (1999).

[21] C. Zener, *Phys. Rev*. 82, 403 (1951).

[22] H. Y. Hwang, S-W. Cheong, N. P. Ong and B. Batlogg, *Phys. Rev. Lett*. 77, 2041 (1996).

[23] Z. W. Chen, S. Tan, Z. R. Yang and Y. H. Zhang, *Phys. Rev. B* 59, 11172 (1999).

[24] Z. R. Yang, S. Tan, Z. W. Chen and Y. H. Zhang, *Phys. Rev. B* 62, 13872 (2000).

[25] G. Srinivasan and M. S. Seehra, *Phys. Rev. B* 28, 1 (1983).

[26] L. Néel, *Proc. Phys. Soc. Sect. A* 65, 869 (1952).

[27] M. F. Hundley and J. J. Neumeier, *Phys. Rev. B* 55, 11511 (1997).

[28] A. P. Ramirez, *J. Phys. Conden. Matt*. 9, 8171 (1997).

[29] M. Rubinstein, D. J. Gillespie, J. E. Snyder and T. M. Tritt, *Phys. Rev. B* 56, 5412 (1997).

[30] Y. Shapira, S. Foner, N. F. Oliveira and T. B. Reed, *Phys. Rev. B* 10, 4765 (1974).

[31] Z. R. Yang, X. Y. Bao, S. Tan and Y. H. Zhang, *Phys. Rev. B* 69, 144407 (2004).

[32] M. Viret, L. Ranno and J. M. D. Coey, *Phys. Rev*. B 55, 8067 (1997).

[33] G. J. Snyder, R. Hiskes, S. DiCarolis, M. R. Beasley and T. H. Geballe, *Phys. Rev. B* 53, 14434 (1996).

[34] S. L. Yuan, W. Y. Zhao, G. Q. Zhang, F. Tu, G. Peng, J. Liu et al., *Appl. Phys. Lett*. 77, 4398 (2000).

[35] F. Rivadulla, M. Freita-Alvite, M. A. López-Quintela, L. E. Hueso, D. R. Miguéns, P. Sande et al., *J. Appl. Phys*. 91, 785 (2002).

[36] D. L. Huber, *J. Appl. Phys*. 83, 6949 (1998).

[37] P. Majumdar and P. Littlewood, *Phys. Rev. Lett*. 81, 1314 (1998).

[38] S.-W. Cheong and M. Mostovoy, *Nat. Mater*. 6, 13 (2007).

[39] M. Fiebig, *J. Phys. D: Appl. Phys*. 38, R123 (2005).

[40] W. Eerenstein, N. D. Mathur and J. F. Scott, *Nature* 442, 759 (2006).

[41] P. K. Baltzer, H. W. Lehmann and M. Robbins, *Phys. Rev. Lett*. 15, 493 (1965).

[42] J. Hemberger, P. Lunkenheimer, R. Fichtl, S. Weber, V. Tsurkan and A. Loidl, *Phys. B: Conden. Matt*. 378–380, 363 (2006).

[43] S. Weber, P. Lunkenheimer, R. Fichtl, J. Hemberger, V. Tsurkan and A. Loidl, *Phys. Rev. Lett*. 96, 157202 (2006).

[44] C. J. Fennie and K. M. Rabe, *Phys. Rev. B* 72, 214123 (2005).

[45] G. Catalan and J. F. Scott, *Nature* 448, E4 (2007).

[46] Y. M. Xie, Z. R. Yang, L. Li, L. H. Yin, X. B. Hu, Y. L. Huang et al., *J. Appl. Phys*. 112, 123912 (2012).

[47] J. R. Macdonald, *Ann. Biomed. Eng*. 20, 289 (1992).

[48] K. S. Cole and R. H. Cole, *J. Chem. Phys*. 9, 341 (1941).

[49] Y. M. Xie, Z. R. Yang, Z. T. Zhang, L. H. Yin, X. L. Chen, W. H. Songet al., *EPL* (Europhysics Letters) 104, 17005 (2013).

[50] W. Li and R. W. Schwartz, *J. Am. Ceram. Soc*. 90, 3536 (2007).

[51] C.-C. Wang, M.-N. Zhang, K.-B. Xu and G.-J. Wang, *J. Appl. Phys*. 112, 034109 (2012).

[52] N. Biškup, A. d. Andrés and J. L. Martinez, *Phys. Rev. B* 72, 024115 (2005).

[53] G. Catalan, *Appl. Phys. Lett*. 88, 102902 (2006).

[54] M. M. Parish and P. B. Littlewood, *Phys. Rev. Lett*. 101, 166602 (2008).

[55] J. Rivas, J. Mira, B. Rivas-Murias, A. Fondado, J. Dec, W. Kleemannet al., *Appl. Phys. Lett*. 88, 242906 (2006).

[56] J. A. Souza, R. F. Jardim, R. Muccillo, E. N. S. Muccillo, M. S. Torikachvili and J. J. Neumeier, *J. Appl. Phys*. 89, 6636 (2001).

[57] V. G. Storchak, J. H. Brewer, P. L. Russo, S. L. Stubbs, O. E. Parfenov, R. L. Lichti et al., *J. Phys. Conden. Matt*. 22, 495601 (2010).

[58] E. L. Nagaev, *Phys. Rep*. 346, 387 (2001).

[59] X. L. Chen, Z. R. Yang, W. Tong, Z. H. Huang, L. Zhang, S. L. Zhang et al., *J. Appl. Phys*. 115, 083916 (2014).

[60] T. Rudolf, C. Kant, F. Mayr, J. Hemberger, V. Tsurkan and A. Loidl, *New J. Phys*. 9, 76 (2007).

[61] F. Yokaichiya, A. Krimmel, V. Tsurkan, I. Margiolaki, P. Thompson, H. N. Bordallo et al., *Phys. Rev. B* 79, 064423 (2009).

[62] Y. Tokura and N. Nagaosa, *Science* 288, 462 (2000).

[63] P. G. Radaelli, *New J. Phys*. 7, 53 (2005).

[64] Z. R. Yang, S. Tan and Y. H. Zhang, *Appl. Phys. Lett*. 79, 3645 (2001).

[65] C. Shen, Z. R. Yang, R. Tong, G. Li, B. S. Wang, Y. P. Sun et al., *J. Magn. Magn. Mater*. 321, 3090 (2009).

[66] V. Tsurkan, V. Fritsch, J. Hemberger, H.-A. K. v. Nidda, N. Büttgen, D. Samusi et al., *J. Phys. Chem. Solids* 66, 2036 (2005).

[67] M. A. Ivanov, V. Y. Mitrofanov, L. D. Falkovskaya and A. Y. Fishman, *J. Magn. Magn. Mater*. 36, 26 (1983).

[68] R. Fichtl, P. Lunkenheimer, J. Hemberger, V. Tsurkan and A. Loidl, *J. Non-Cryst. Solids* 351, 2793 (2005).